Supplementary Information

Strategically designed deep-ultraviolet optical crystals with balanced properties by small heteroatom substitution

Mei Hu[a#], Zhencheng Wu[b#], Xin Su[b], Hongheng Chen[a], Qun Jing[a*], Zhaohui Chen[c*], and Ming-Hsien Lee[d]

[a]Xinjiang Key Laboratory of Solid State Physics and Devices, School of Physical Science and Technology, Xinjiang University, 777 Huarui Street, Urumqi 830017, China;

[b]Xinjiang Key Laboratory of Phase Transitions and Microstructures in Condensed Matter Physics, College of Physical Science and Technology, Yili Normal University, Yining 835000, China;

[c]Key Laboratory of Oil & Gas Fine Chemicals, Ministry of Education & Xinjiang Uyghur Autonomous Region, School of Chemical Engineering and Technology, Xinjiang University, 777 Huarui Street, Urumqi 830017, China;

[d]Department of Physics, Tamkang University, New Taipei City 25137, China.

[#]These authors contribute equally.

*Corresponding author (email: qunjing@xju.edu.cn; chenzhaohui@xju.edu.cn)

Table of Contents

Figure S4. Hirshfeld surface plotted of α-$C(NH_2)_3SO_3NH_2$: (a) d_{norm}, (b) shape index, and (e)-(f) 2D fingerprint plots for overall interactions and individual interactions of atom types in crystal packing of α-$C(NH_2)_3SO_3NH_2$. Hirshfeld surface plotted of β-$C(NH_2)_3SO_3NH_2$: (c) d_{norm}, (d) shape index, and (g)-(h) 2D fingerprint plots.

Figure S5. 2D Fingerprint plots for (a) overall interactions and (b–i) individual interactions of atom types in the crystal packing of α-$C(NH_2)_3SO_3NH_2$. Here, d_e and d_i represent distances from the Hirshfeld surfaces to the nearest nucleus outside and inside the surface, respectively.

Figure S6. 2D Fingerprint plots for (a) overall interactions and (b–i) individual interactions of atom types in the crystal packing of β-$C(NH_2)_3SO_3NH_2$. Here, d_e and d_i represent distances from the Hirshfeld surfaces to the nearest nucleus outside and inside the surface, respectively.

Figure S7. GGA-PBE band structure of (a) α-$C(NH_2)_3SO_3NH_2$ and (c) β-$C(NH_2)_3SO_3NH_2$.

Figure S8. The measurement of birefringence (a) The interference color α-$C(NH_2)_3SO_3NH_2$ and (e) β-$C(NH_2)_3SO_3NH_2$; The thickness of (b) α-$C(NH_2)_3SO_3NH_2$ and (f) β-$C(NH_2)_3SO_3NH_2$ crystal under the polarizing microscope; A α-$C(NH_2)_3SO_3NH_2$ single crystal under the (c) positive (up) and (d) negative (down) compensatory rotation; A β-$C(NH_2)_3SO_3NH_2$ single crystal under the (g) positive (up) and (h) negative (down) compensatory rotation.

Figure S9. Phase-matched wavelengths of β-$C(NH_2)_3SO_3NH_2$.

Figure S10. The PDOS of α-$C(NH_2)_3SO_3NH_2$.

Figure S11. (a)The PDOS of β-$C(NH_2)_3SO_3NH_2$. (b) The occupied states of virtual-electron (VE) and unoccupied states of virtual-hole (VH) of β-$C(NH_2)_3SO_3NH_2$. The contribution of VE is 0.81 pm/V, the contribution of VH is -0.09 pm/V, and the total contribution is 0.72 pm/V. Therefore, the contribution of VE is greater than 70%.

1. Experimental Section

Crystal Preparation. Single crystals of *α*/*β*-$C(NH_2)_3SO_3NH_2$ were synthesized by a simple slow aqueous solution evaporation method. The mixtures of $[C(NH_2)_3]_2CO_3$: HSO_3NH_2 = 1:2 (*α*-$C(NH_2)_3SO_3NH_2$) and $[C(NH_2)_3]_2CO_3$: HSO_3NH_2 : $NH_4SO_3NH_2$ = 1 : 2 : 1 (*β*-$C(NH_2)_3SO_3NH_2$) were weighed in molar ratios, respectively, and dissolved in a conical flasks containing 60 mL of deionized water. Subsequently, the conical flask was placed on a magnetic stirrer at 60 °C for two hours to fully dissolve the mixture for the reaction. After mixing, the conical flask was placed in a room-temperature environment, and after a few days of slow evaporation, colorless and transparent crystals are successfully obtained.

The polycrystalline samples of *β*-$C(NH_2)_3SO_3NH_2$ were prepared using the same slow evaporation method. Note that unlike *β*-$C(NH_2)_3SO_3NH_2$, the polycrystalline powder of *α*-$C(NH_2)_3SO_3NH_2$ was prepared directly by grinding its single crystals. Separately, the obtained *α*-$C(NH_2)_3SO_3NH_2$ (as raw material) was dissolved in 40 mL of deionized water and slowly evaporated at 70 °C in an oven. After these steps, powder XRD analysis confirmed the phase purity of the polycrystalline samples, *α*/*β*-$C(NH_2)_3SO_3NH_2$ (Fig. S1 in the Supporting Information (SI)). These polycrystalline samples were used for subsequent performance testing.

Single-crystal XRD. The single-crystal XRD data were collected on a Bruker D8 Venture diffractometer using Mo K*α* radiation (λ = 0.71073 Å). All data were integrated with SAINT, and absorption correction was not applied (SADABS). The crystal structure models were then solved and refined on the SHELXTL and Olex2 packages using the intrinsic phase method and the full-matrix least-squares technique.[1] All non-hydrogen atoms were refined with anisotropic displacement parameters. The heteroatom-bound hydrogen atoms were refined with isotropic displacement parameters.[2] The absence of higher symmetry in the crystal structure was confirmed using PLATON software.[3] Crystallographic data and structural refinements for *α*-$C(NH_2)_3SO_3NH_2$ and *β*-$C(NH_2)_3SO_3NH_2$ are listed in Table S2; atomic coordinates, isotropic or equivalent

displacement parameters, selected bond distances and angles, and anisotropic displacement parameters are summarized in Tables S3-S8, respectively.

Powder X-ray diffraction (XRD). The determination of the pure sample was carried out using powder XRD, which was carried out with a Bruker D2 PHASER diffractometer at room temperature using Cu Kα radiation with λ = 1.5418 Å. The diffraction patterns were recorded with the 2θ range of 10-70° with a scan step width of 0.02°, and a scan rate of 1 s/step.

Thermal Analysis. The thermal performance of α-$C(NH_2)_3SO_3NH_2$ and β-$C(NH_2)_3SO_3NH_2$ was evaluated using a HITACHI STA7300. Thermogravimetric analyzer under a nitrogen atmosphere over a temperature range of 30–700 °C. Their stability was determined by recording its thermodynamic behavior.

Infrared and UV-Vis-NIR Diffuse Reflectance Spectroscopy. Infrared spectra in the range of 400 to 4000 cm^{-1} were recorded at room temperature using a BRUKER VERTEX 70 FTIR spectrometer for verification of structural units. Before the measurement, the sample was mixed with dry KBr at a mass ratio of 1:100, ground thoroughly, and then pressed into a transparent pellet for measurement.

The UV-Vis-NIR diffuse reflectance data were collected at room temperature using a Shimadzu SolidSpec-3700DUV spectrophotometer. Data were collected in the wavelength range of 180-1500 nm.

Powder Second Harmonic Generation (SHG) Measurements. The SHG responses were quantitatively measured through the Kurtz-Perry powder technique employing an SHG-HighRes-100 spectrometer (Voyawave Optics), with a Q-switched Nd : YAG laser (1064 nm) as the excitation source. The process was then repeated using a standard NLO material, the KH_2PO_4 (KDP), and the second harmonic output intensities of the samples were compared with those of KDP. Additionally, because the samples absorbing moisture easily, it is difficult to sieve sufficient quantities of particles with different size distributions for phase-matching curve measurements.

Experimental Birefringence. For experimental measurements of the birefringence, a ZEISS Axio Scope 5 pol model polarizing microscope equipped with a Berek compensator was used. The wavelength of the light source was 546 nm. Based on

theoretical knowledge, the formula for calculating birefringence is provided.[4] $R = |N_g - N_p| \times d = \Delta n \times d$, where R represents the optical path difference; N_g and N_p refer to the refractive indices of the slow and fast rays, respectively; Δn represents the difference value of the refractive index (birefringence); d represents the thickness of the crystal.

2. Computational Methods

The electronic structures and optical properties of *α*/*β*-$C(NH_2)_3SO_3NH_2$ were calculated using the first-principles method implemented in the CASTEP code.[5-7] During the calculation, the Perdew−Burke−Ernzerhof (PBE) functional[8] and the norm-conserving pseudopotential (NCP)[8, 9] were used, and the valence electron configurations were assigned as C $2s^2 2p^2$, N $2s^2 2p^3$, H $1s^1$, S $3s^2 3p^4$, and O $2s^2 2p^4$. The plane wave cutoff energy for *α*/*β*-$C(NH_2)_3SO_3NH_2$ was set to 830 eV. Using the Monkhorst-Pack method, the *K* points of the two compounds were finally set to the appropriate values of 3 × 2 × 3 (*α*-$C(NH_2)_3SO_3NH_2$) and 4 × 3 × 3 (*β*-$C(NH_2)_3SO_3NH_2$).[10] To achieve convergence in geometry optimization, the total energy convergence criterion was set to 5.0×10^{-6} eV, and the convergence criteria for maximum atomic force, maximum stress, and maximum displacement were set to 0.01 eV/Å, 0.02 GPa, and 5.0×10^{-4} Å, respectively. All other calculation parameters and convergence criteria were set to the default values of the CASTEP software package. Considering the underestimation of band gap caused by the discontinuity of the GGA functional, the HSE06 method[11-13] implemented in the PWmat[14, 15] code was used to obtain band gap for comparison with experimental values.

Based on the obtained electronic structures, the imaginary part (ε_2) of the dielectric constant of the crystal was obtained using the following expression:

$$\varepsilon_2 = \frac{2e^2\pi}{\Omega\varepsilon_0}\sum_{k,v,c} |<\varphi_\kappa^c|u\cdot r|\varphi_\kappa^v>|^2 \delta\left(\mathrm{E}_\kappa^c - \mathrm{E}_\kappa^v - \mathrm{E}\right)$$

where Ω is the unit cell volume, *v, c* are the valence and conduction bands of the crystal, respectively, and *u* is the vector of the direction of the electric field of the incident light. The real part of the dielectric constant (ε_1) can be further obtained by

the Kramer-Kronig transformation.[16] Then the scissors operator was applied to obtain the refractive indices and birefringence. The scissors corrections were 1.911 eV (for the *α* phase) and 1.595 eV (for the *β* phase), respectively.

The SHG tensors were further calculated using the formula originally proposed by Rashkeev and Lin *et al*. and then revised by Zhang *et al*.[17-19] The SHG tensors were calculated using the formula:

$$\chi^{(2)}_{\alpha\beta\gamma} = \chi^{(2)}_{\alpha\beta\gamma}(VE) + \chi^{(2)}_{\alpha\beta\gamma}(VH) \quad (1)$$

$$\chi^{(2)}_{\alpha\beta,\gamma}(VE) = \frac{e^3}{2\hbar m^3}\sum_{vcc'}\int\frac{d^3k}{4\pi^3}P(\alpha\beta\gamma)Im[P^{\alpha}_{cv}P^{\beta}_{cc'}P^{\gamma}_{c'v}] \times \left(\frac{1}{\omega^3_{cv}\omega^2_{vc'}}+\frac{2}{\omega^4_{vc}\omega_{c'v}}\right) \quad (2)$$

$$\chi^{(2)}_{\alpha\beta\gamma}(VH) = \frac{e^3}{2\hbar m^3}\sum_{vv'c}\int\frac{d^3k}{4\pi^3}P(\alpha\beta\gamma)Im[P^{\alpha}_{vv'}P^{\beta}_{cv}P^{\gamma}_{cv}] \times \left(\frac{1}{\omega^3_{cv}\omega^2_{v'c}}+\frac{2}{\omega^4_{vc}\omega_{cv'}}\right) \quad (3)$$

Here, α, β, and γ are Cartesian components, v and v' denote valence bands, c and c' denotes conduction bands, and $P(\alpha\beta\gamma)$ denotes full permutation. The band energy difference and momentum matrix elements are denoted as $\hbar\omega_{ij}$ and P^{α}_{ij}, respectively. Employing scissor corrections, reliable SHG coefficients can be obtained from the GGA calculations. The effective SHG coefficient was evaluated using the formula first suggested by Kurtz-Perry[21] and Cyvin *et al.*[22] and later revised by Cheng *et al.*[23]:

$$\langle(d^{2\omega}_{eff})^2\rangle = \frac{19}{105}\sum_a (d^{2\omega}_{aaa})^2 + \frac{13}{105}\sum_{a\neq b} d^{2\omega}_{aaa}d^{2\omega}_{abb} + \frac{44}{105}\sum_{a\neq b}(d^{2\omega}_{aab})^2 + \frac{13}{105}\times\sum_{abc,\,cyclic} d^{2\omega}_{aab}d^{2\omega}_{bcc} + \frac{5}{7}(d^{2\omega}_{abc})^2$$

Since *β*-$C(NH_2)_3SO_3NH_2$ crystallizes in the noncentrosymmetric space group *Iba*2, which belongs to the mm2 point group, it has three independent SHG tensors d_{15}, d_{24}, and d_{33}, the effective SHG response can be calculated as:

$$<\left(d^{2\omega}_{eff}\right)^2>=\frac{19}{105}\left(d^{2\omega}_{33}\right)^2+\frac{13}{105}\left(d^{2\omega}_{33}d^{2\omega}_{15}+d^{2\omega}_{33}d^{2\omega}_{24}\right)+\frac{44}{105}\left(\left(d^{2\omega}_{15}\right)^2+\left(d^{2\omega}_{24}\right)^2\right)+\frac{13}{105}d^{2\omega}_{24}d^{2\omega}_{15}$$

The contribution of the functional basic units to the birefringence and SHG was analyzed using the real space atom-cutting (RSAC) method. The RSAC method refers to the division of real space into multiple regions, with each region containing one ion.[17] When the wavefunction belonging to a specific ion or group is defined as zero (referred to as “cutting”), it is considered that the contribution of the ion or group has

been removed. Using this method, the contribution from ions or groups can be detected. For instance, if we wish to obtain the contribution ($\chi^{(n)}(A)$) of a certain ion A to the n-th order polarizability, we can do so by excluding all other ions except for ion A from the compound, which can be expressed as $\chi^{(n)}(A)$ = $\chi^{(n)}$(All ions except A are cut). For simplicity, each region was defined as a sphere centered on a specific ion. According to the principle that the cutting spheres touch but do not overlap, the atomic cutting radii were set as follows: C: 0.77 Å, N: 0.75 Å, H: 0.32 Å, S: 1.02 Å, O: 0.65 Å.

Table S1. Cutoff edge wavelengths for some S-containing compounds (containing planar units).

Compound	λ_{cutoff}/nm	Ref.
SO_4		
$(C(NH_2)_3)Al(SO_4)_2(H_2O)_6$	228	24
$Zn(C(NH_2)_3)_2(SO_4)_2$	261	25
$Zn(SO_4)(CH_4N_2S)_3$	300	26
$(C_2H_{12}N_6)Zn(SO_4)_2$	259	27
$[C(NH_2)_3]BiCl_2SO_4$	322	28
$La_2B_3O_4(OH)_3(SO_4)_2$	455	29
SO_3NH_2		
$C_3N_6H_7SO_3NH_2$	206	30
$Sr(NO_3)(NH_2SO_3)\cdot H_2O$	231	31
$[C_2N_4H_7O][NH_2SO_3]$	227	32
$C_2H_5N_4O_2S_2(H_2O)Cl$	345	33
$[(C_4H_6N_3)(NH_2SO_3)]$-II	333	34
$C_4N_3H_6SO_3NH_2$-I	350	35
$[(C_4H_6N_3)(NH_2SO_3)]$-III	350	36
SO_3CF_3		
$C(NH_2)_3(CF_3SO_3)$	183	37
$[(C_4H_7N_3)(CF_3SO_3)_2]$	324	34
$(C_4H_5N_3)(C_4H_6N_3)(CF_3SO_3)$	360	36
SO_3CH_3		
$C(NH_2)_3CH_3SO_3$	190	38
$C_2H_5N_4O_2S_2(CH_3O_3S)$	366	33
$(C_5H_6NO)(CH_3SO_3)$	252	39
$[(C_4H_5N_3)(C_4H_6N_3)(CH_3SO_3)]$	330	34
$(C_4H_6N_3)(CH_3SO_3)$	360	36
SO_3F		
$C(NH_2)_3SO_3F$	200	40
SO_3S		
$[C(NH_2)_3]_2SO_3S$	254	41
$Na_{10}Cd(NO_3)_4(SO_3S)_4$	331	42
$[C(NH_2)_3]S_3O_6$	218	43
$[C(NH_2)_3]_2S_2O_8$	222	44
$[C(NH_2)_3]_2S_2O_6$	237	45

As shown in Table S1, large π-conjugated groups may be unfavorable for the cutoff edge blueshift. Meanwhile, there are still many gaps to be explored for S-containing compounds that combinre π-conjugated and non-π-conjugated groups through investigation.

Table S2. Crystal data and structure refinement for *α/β*-$C(NH_2)_3SO_3NH_2$.

Empirical formula	*α*-$C(NH_2)_3SO_3NH_2$	*β*-$C(NH_2)_3SO_3NH_2$
Formula weight	156.17	156.17
Temperature [K]	273.15	273.15
Crystal system	monoclinic	orthorhombic
Space group	$P2_1/c$ (14)	$Iba2$ (45)
a [Å]	7.404(5)	13.162(2)
b [Å]	9.898(7)	9.6507(17)
c [Å]	8.567(6)	9.7932(17)
α [°]	90	90
β [°]	99.82(3)	90
γ [°]	90	90
Volume [Å]	618.6(8)	1092.45(6)
Z	4	4
ρ_{calc} [g/cm^3]	1.677	1.668
μ [mm^{-1}]	0.468	0.466
F (000)	328	656
2θ range [°]	5.58 to 54.97	5.23 to 54.94
Index ranges	$-9 \le h \le 9, -10 \le k \le 12, -11 \le l \le 11$	$-16 \le h \le 16, -12 \le k \le 12, -12 \le l \le 12$
Reflections collected	4912	3919
Independent reflections	1406 [*R*(int) = 0.0730]	1362 [*R*(int) = 0.0595]
Completeness to theta	99.9 %	98.7 %
Data/restraints/parameters	1406 / 0 / 89	1362 / 1 / 90
Goodness-of-fit on F^2	1.073	1.117
Final *R* indexes [$F_o^2 > 2\sigma(F_o^2)$] [a]	$R_1 = 0.0518$, $wR_2 = 0.1185$	$R_1 = 0.0469$, $wR_2 = 0.0827$
R indexes (all data) [a]	$R_1 = 0.0785$, $wR_2 = 0.1454$	$R_1 = 0.0756$, $wR_2 = 0.0998$
Largest peak/hole [eÅ^{-3}]	0.42/−0.42	0.30/−0.34

[a] $R_1 = \Sigma||F_o| - |F_c||/\Sigma|F_o|$ and $wR_2 = [\Sigma w(F_o^2 - F_c^2)^2/\Sigma wF_o^4]^{1/2}$ for $F_o^2 > 2\sigma(F_o^2)$

Table S3. Atomic coordinates (× 10^4) and equivalent isotropic displacement parameters (Å^2 × 10^3) for α-$C(NH_2)_3SO_3NH_2$.

Atom	*x*	*y*	*z*	U_{eq}[a]
S1	1.90196(10)	0.44241(9)	0.20802(9)	0.0290(3)
N1	1.4170(4)	0.4349(3)	0.3196(4)	0.0437(8)
N2	1.2856(4)	0.2866(3)	0.4729(4)	0.0434(8)
N3	1.5816(4)	0.2548(3)	0.4348(4)	0.0518(10)
N4	2.0430(4)	0.5719(3)	0.2364(4)	0.0339(7)
C1	1.4282(4)	0.3254(4)	0.4091(4)	0.0362(8)
O1	1.9834(3)	0.3540(2)	0.1044(3)	0.0358(6)
O2	1.9062(3)	0.3869(3)	0.3656(3)	0.0385(6)
O3	1.7178(3)	0.4854(3)	0.1365(3)	0.0405(7)
H1A	1.509598	0.459992	0.278360	0.052
H1B	1.317139	0.480993	0.302736	0.052
H2A	1.293098	0.215326	0.531114	0.052
H2B	1.185661	0.332592	0.456078	0.052
H3A	1.674087	0.280112	0.393429	0.062
H3B	1.589163	0.183572	0.492985	0.062
H4A	2.041(5)	0.608(4)	0.146(5)	0.041
H4B	2.028(5)	0.628(4)	0.307(5)	0.041

[a]U_{eq} is defined as 1/3 of the trace of the orthogonalized U_{ij} tensor.

Table S4. Atomic coordinates (× 10^4) and equivalent isotropic displacement parameters (Å^2 × 10^3) for β-$C(NH_2)_3SO_3NH_2$.

Atom	*x*	*y*	*z*	U_{eq}[a]
S1	0.74371(10)	0.49916(17)	0.64517(17)	0.0255(4)
N1	0.5668(4)	0.3390(6)	0.3876(6)	0.0394(13)
N2	0.4035(4)	0.2610(6)	0.3863(7)	0.0406(14)
N3	0.5130(5)	0.1942(6)	0.2171(6)	0.0421(15)
N4	0.8239(5)	0.5871(6)	0.5520(7)	0.0359(15)
C1	0.4948(5)	0.2646(7)	0.3302(5)	0.0303(14)
O1	0.7727(3)	0.3561(4)	0.6258(5)	0.0362(11)
O2	0.6405(3)	0.5278(5)	0.6006(4)	0.0342(11)
O3	0.7616(3)	0.5493(5)	0.7830(4)	0.0352(11)
H1A	0.554305	0.384806	0.461010	0.047
H1B	0.626377	0.341909	0.351625	0.047
H2A	0.391627	0.307060	0.459777	0.049
H2B	0.356054	0.212594	0.349399	0.049
H3A	0.572377	0.196785	0.180414	0.050
H3B	0.465568	0.145771	0.180134	0.050
H4A	0.827(6)	0.551(8)	0.488(7)	0.043
H4B	0.805(6)	0.655(8)	0.546(8)	0.043

[a]U_{eq} is defined as 1/3 of the trace of the orthogonalized U_{ij} tensor.

Table S5. Anisotropic displacement parameters (Å^2×10^3) for α-C(NH$_2$)$_3$SO$_3$NH$_2$. The anisotropic displacement factor exponent takes the form: -2π^2[h^2(a*)^2U_{11}+ k^2(b*)^2U_{22} +...+2hka*b*U_{12}].

Atom	U_{11}	U_{22}	U_{33}	U_{23}	U_{13}	U_{12}
S1	0.0256(4)	0.0285(5)	0.0332(5)	−0.0002(3)	0.0060(3)	−0.0004(3)
O2	0.0410(13)	0.0410(15)	0.0354(14)	0.0073(12)	0.0117(11)	−0.0031(11)
O1	0.0419(13)	0.0283(13)	0.0396(14)	−0.0065(10)	0.0139(11)	0.0044(10)
O3	0.0247(12)	0.0413(15)	0.0536(16)	0.0006(12)	0.0015(11)	−0.0017(11)
N4	0.0321(14)	0.0336(18)	0.0363(16)	−0.0044(13)	0.0068(13)	−0.0042(13)
N2	0.0282(14)	0.0452(19)	0.057(2)	0.0138(16)	0.0063(13)	−0.0012(13)
N1	0.0271(15)	0.045(2)	0.060(2)	0.0144(16)	0.0098(14)	0.0040(13)
N3	0.0315(16)	0.048(2)	0.077(3)	0.0225(19)	0.0127(16)	0.0073(15)
C1	0.0298(16)	0.034(2)	0.043(2)	0.0009(15)	0.0008(14)	−0.0048(15)

Table S6. Anisotropic displacement parameters (Å^2×10^3) for β-C(NH$_2$)$_3$SO$_3$NH$_2$. The anisotropic displacement factor exponent takes the form: -2π^2[h^2(a*)^2U_{11}+ k^2(b*)^2U_{22} +...+2hka*b*U_{12}].

Atom	U_{11}	U_{22}	U_{33}	U_{23}	U_{13}	U_{12}
S1	0.0260(7)	0.0223(6)	0.0281(6)	−0.0011(6)	−0.0009(8)	−0.0007(8)
O1	0.034(2)	0.023(2)	0.051(3)	−0.002(2)	0.003(2)	0.002(2)
O2	0.022(2)	0.038(3)	0.042(2)	0.001(2)	−0.0051(17)	0.000(2)
O3	0.039(3)	0.038(3)	0.028(2)	−0.0039(19)	−0.006(2)	−0.005(2)
N1	0.032(3)	0.047(3)	0.039(3)	−0.004(3)	−0.002(3)	−0.008(3)
N2	0.034(3)	0.049(3)	0.039(3)	−0.013(3)	0.006(3)	−0.007(3)
N3	0.032(3)	0.048(4)	0.046(3)	−0.016(3)	0.005(3)	−0.004(3)
N4	0.036(4)	0.030(3)	0.043(3)	0.002(3)	0.001(3)	0.001(3)
C1	0.029(4)	0.030(3)	0.033(3)	0.005(3)	0.001(3)	−0.004(3)

Table S7. Selected bond lengths [Å] and angles (°) for α-$C(NH_2)_3SO_3NH_2$.

Atom–Atom	Length [Å]	Atom–Atom	Length [Å]
S1–O2	1.453(3)	N2–C1	1.326(4)
S1–O1	1.449(2)	N1–H1A	0.8600
S1–O3	1.460(2)	N1–H1B	0.8600
S1–N4	1.644(3)	N1–C1	1.321(5)
N4–H4A	0.85(4)	N3–H3A	0.8600
N4–H4B	0.84(4)	N3–H3B	0.8600
N2–H2A	0.8600	N3–C1	1.320(4)
N2–H2B	0.8600		
Atom–Atom–Atom	Angle [°]	Atom–Atom–Atom	Angle [°]
O2–S1–O3	111.76(14)	C1–N2–H2B	120.0
O2–S1–N4	104.17(16)	H1A–N1–H1B	120.0
O1–S1–O2	113.27(16)	C1–N1–H1A	120.0
O1–S1–O3	112.08(15)	C1–N1–H1B	120.0
O1–S1–N4	103.96(15)	H3A–N3–H3B	120.0
O3–S1–N4	111.03(16)	C1–N3–H3A	120.0
S1–N4–H4A	107(3)	C1–N3–H3B	120.0
S1–N4–H4B	118(3)	N1–C1–N2	120.1(3)
H4A–N4–H4B	113(4)	N3–C1–N2	120.0(3)
H2A–N2–H2B	120.0	N3–C1–N1	119.9(3)
C1–N2–H2A	120.0		

Table S8. Selected bond lengths [Å] and angles (°) for β-$C(NH_2)_3SO_3NH_2$.

Atom–Atom	Length [Å]	Atom–Atom	Length [Å]
S1–O1	1.445(4)	N2–H2B	0.8600
S1–O2	1.453(4)	N2–C1	1.321(8)
S1–O3	1.453(4)	N3–H3A	0.8600
S1–N4	1.633(7)	N3–H3B	0.8600
N1–H1A	0.8600	N3–C1	1.322(8)
N1–H1B	0.8600	N4–H4A	0.72(7)
N1–C1	1.315(8)	N4–H4B	0.71(8)
N2–H2A	0.8600	Atom–Atom–Atom	Angle [°]
Atom–Atom–Atom	Angle [°]	C1–N2–H2A	120.0
O1–S1–O2	112.9(3)	C1–N2–H2B	120.0
O1–S1–O3	113.4(3)	H3A–N3–H3B	120.0
O1–S1–N4	104.6(3)	C1–N3–H3A	120.0
O2–S1–O3	111.5(3)	C1–N3–H3B	120.0
O2–S1–N4	109.7(3)	S1–N4–H4A	106(7)
O3–S1–N4	103.9(3)	S1–N4–H4B	107(7)
H1A–N1–H1B	120.0	H4A–N4–H4B	113(9)
C1–N1–H1A	120.0	N1–C1–N2	119.5(6)
C1–N1–H1B	120.0	N1–C1–N3	120.5(7)
H2A–N2–H2B	120.0	N2–C1–N3	120.0(7)

Table S9. The cutoff edge wavelengths (λ_{cutoff}) of optical crystal materials containing $[C(NH_2)_3]$ or $[SO_3NH_2]$.

Compound	λ_{cutoff}/nm	Ref.
$Cs_2Mg(NH_2SO_3)_4 \cdot 4H_2O$	180	46
$[C(NH_2)_3(CF_3SO_3)]$	183	37
β-$C(NH_2)_3SO_3NH_2$	190	This work
$[C(NH_2)_3][B_3O_3F_2(OH)_2]$	190	47
$C(NH_2)_3CH_3SO_3$	190	38
$Ba(NH_2SO_3)_2$	190	48
$KCd(NH_2SO_3)_3$	190	49
α-$C(NH_2)_3SO_3NH_2$	190	This work
$Sr(NH_2SO_3)_2$	190	48
$C(NH_2)_3BF_4$	193	50
$[C(NH_2)_3]_2[B_4O_5(OH)_4]\cdot 2H_2O$	194	51
$[C(NH_2)_3]_2[B_3O_3F_4(OH)]$	195	47
$(NH_4)[C(NH_2)_3][B_3O_3F_4(OH)]$	195	52
$C(NH_2)_3B_5O_6(OH)_4\cdot H_2O$	197	51
$Rb_2Ca(NH_2SO_3)_4$	200	46
$K_2Ca(NH_2SO_3)_4$	200	46
$C(NH_2)_3ClO_4$	200	53
$C(NH_2)_3SO_3F$	200	40
$[C(NH_2)_3]_6(PO_4)_2\cdot 3H_2O$	205	54
$Ca(NH_2SO_3)_2\cdot H_2O$	206	55
$C_3N_6H_7SO_3NH_2$	206	30
$Pb(NH_2SO_3)_2$	208	55
$[C(NH_2)_3]_2Zn(CO_3)_2$	210	56
$Cd(NH_2SO_3)_2\cdot 2H_2O$	210	57
$[C(NH_2)_3]_3AsO_4\cdot 2H_2O$	210	58
$Cd(NH_2SO_3)_2$	212	57
$[C(NH_2)_3][B(C_2O_2H_4)_2]$	215	59
$[C(NH_2)_3]S_3O_6$	218	43
$[C(NH_2)_3]_2S_2O_8$	222	44
$Ca(NH_2SO_3)_2\cdot 4H_2O$	224	55
$Pb(NH_2SO_3)_2\cdot H_2O$	226	55
$[C_2N_4H_7O][NH_2SO_3]$	227	32
$C(NH_2)_3IO_2F_2$	230	60
$Sr(NO_3)(NH_2SO_3)\cdot H_2O$	231	31
$C(NH_2)_3Sb_2F_7$	236	61
$[C(NH_2)_3]_2S_2O_6$	237	45
$C(NH_2)_3IO_3$	240	62
$C(NH_2)_3SbF_4$	241	61
$C(NH_2)_3Sb_3F_3(HPO_3)_4$	243	63
$(C(NH_2)_3)_2(I_2O_5F)(IO_3)(H_2O)$	246	60

$[C(NH_2)_3]_3PO_4 \cdot 2H_2O$	250	64
$[C(NH_2)_3]_2SO_3S$	254	41
$[C(NH_2)_3]_3VO_4 \cdot 2H_2O$	285	58
$[C(NH_2)_2NHNO_2][C(NH_2)_3](NO_3)_2$	298	65
$[C(NH_2)_3]Sb(C_2O_4)F_2 \cdot H_2O$	303	66
$C(NH_2)_3(I_3O_8)(HI_3O_8)(H_2I_2O_6)(HIO_3)_4 \cdot 3H_2O$	304	67
$Hg_2(C(NH_2)_3)Cl_5$	306	68
$[C(NH_2)_3]_6Mo_7O_{24}$	313	69
$[C(NH_2)_3]_{10}(MoO_3)_{10}(PO_4)_2(HPO_4)_2 \cdot 5H_2O$	316	70
$[C(NH_2)_3]BiCl_2SO_4$	322	28
$C(NH_2)_3MoO_3(IO_3)$	330	71
$C(NH_2)_3Cd(C_2O_4)Cl(H_2O) \cdot H_2O$	330	72
$[(C_4H_6N_3)(NH_2SO_3)]$-II	333	34
$[C(NH_2)_3]_3C_3N_3S_3$	340	73
$C(NH_2)_3Rb(I_3O_8)(IO_3)(I_2O_6H_2)$	350	74
$C_4N_3H_6SO_3NH_2$-I	350	35
$[(C_4H_6N_3)(NH_2SO_3)]$-III	350	36
$[C(NH_2)_3]SbFPO_4 \cdot H_2O$	358	63
$C(NH_2)_3(HC_4O_4)$	370	75
$[C(NH_2)_3]_3V_2O_4F_5$	377	76

Table S10. The cutoff edge wavelengths, SHG and birefringence of nonlinear optical crystal materials containing $[C(NH_2)_3]$ or $[SO_3NH_2]$.

Compound	λ_{cutoff}/nm	SHG× KDP	Birefringence	Ref.
$KBe_2BO_3F_2$ (KBBF)	147	1.2	0.072@1064nm	77
LiB_3O_5 (LBO)	158	3	0.039@1064nm	78
$CsLiB_6O_{10}$ (CLBO)	180	2.2	0.049@1064nm	79
$Cs_2Mg(NH_2SO_3)_4 \cdot 4H_2O$	180	2.3	0.054@546.1nm	1
β-BaB_2O_4 (BBO)	185	5.6	0.113@1064nm	80
β-$C(NH_2)_3SO_3NH_2$	190	1.41	0.74@1064nm	This work
$[C(NH_2)_3][B_3O_3F_2(OH)_2]$	190	0.9	0.173@1064nm	4
$Ba(NH_2SO_3)_2$	190	2.7	0.03@1064nm	6
$Sr(NH_2SO_3)_2$	190	1.2	0.03@1064nm	9
$[C(NH_2)_3]_2[B_3O_3F_4(OH)]$	195	1.4	0.161@1064nm	12
$C(NH_2)_3SO_3F$	200	5	0.133@1064nm	18
$[C(NH_2)_3]_6(PO_4)_2 \cdot 3H_2O$	205	3.8	0.078@546nm	19
$Ca(NH_2SO_3)_2 \cdot H_2O$	206	0.3	0.033@1064nm	20
$[C(NH_2)_3]_2Zn(CO_3)_2$	210	0.5		56
$[C(NH_2)_3]_3AsO_4 \cdot 2H_2O$	210	0.9	0.0387@546nm	25
$Cd(NH_2SO_3)_2$	212	0.15	0.037@1064nm	26
$[C(NH_2)_3][B(C_2O_2H_4)_2]$	215	0.7	0.078@550nm	27
$[C(NH_2)_3]S_3O_6$	218	1.4	0.097@546nm	28
$[C_2N_4H_7O][NH_2SO_3]$	227	6.2	0.225@1064nm	32
$Sr(NO_3)(NH_2SO_3) \cdot H_2O$	231	5.1	0.0665@532nm	34
$[C(NH_2)_3]_3PO_4 \cdot 2H_2O$	250	1.5	0.055@546.1nm	64
$[C(NH_2)_3]_2SO_3S$	254	2.8	0.073@546nm	42
$[C(NH_2)_3]_3VO_4 \cdot 2H_2O$	285	2.2	0.086@1064nm	43
$[C(NH_2)_2NHNO_2][C(NH_2)_3](NO_3)_2$	298	1.5	0.09@550nm	44
$C(NH_2)_3(I_3O_8)(HI_3O_8)(H_2I_2O_6)(HIO_3)_4 \cdot 3H_2O$	304	2.1	0.06@550nm	46
$[C(NH_2)_3]_6Mo_7O_{24}$	313	1.3	203@550nm	48
$[C(NH_2)_3]_{10}(MoO_3)_{10}(PO_4)_2(HPO_4)_2 \cdot 5H_2O$	316		0.158@550nm	49
$[C(NH_2)_3]_3C_3N_3S_3$	340	2	0.067@550nm	73
$C_4N_3H_6SO_3NH_2$-I	350	2.5	0.233@546nm	56

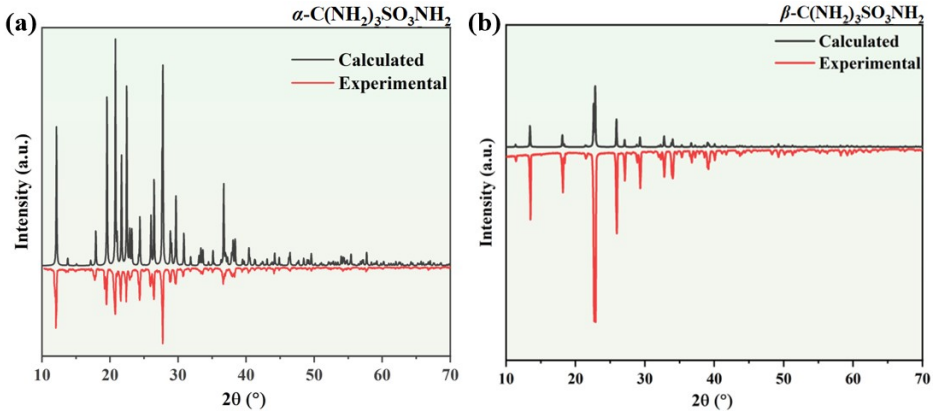

Figure S1. Calculated and experimental XRD patterns of (a) α-$C(NH_2)_3SO_3NH_2$ and (b) β-$C(NH_2)_3SO_3NH_2$.

The agreement between theoretical and experimental XRD patterns confirms the purity of the α/β-$C(NH_2)_3SO_3NH_2$ polycrystalline powders (Figure S1). This is a prerequisite for ensuring the accuracy of the subsequent test results.

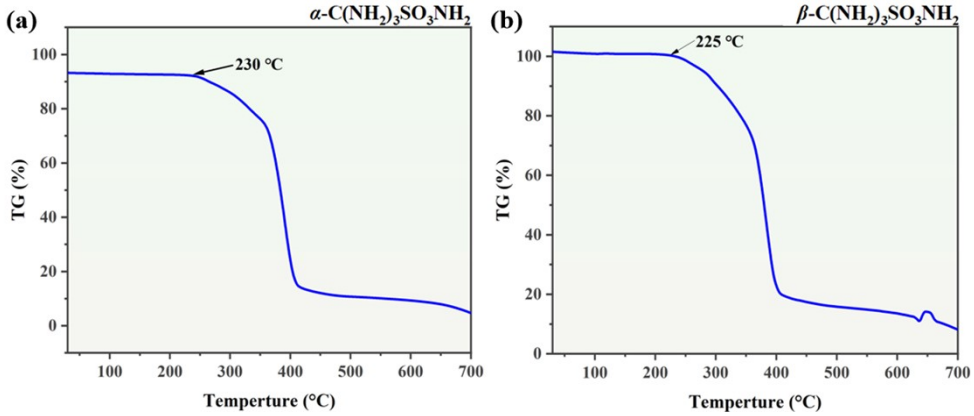

Figure S2. Thermogravimetric curve of (a) α-$C(NH_2)_3SO_3NH_2$ and (b) β-$C(NH_2)_3SO_3NH_2$.

Thermogravimetric test results show that α-$C(NH_2)_3SO_3NH_2$ and β-$C(NH_2)_3SO_3NH_2$ decompose at about 230 °C and 225 °C, respectively, indicating thermal stability up to this temperature.

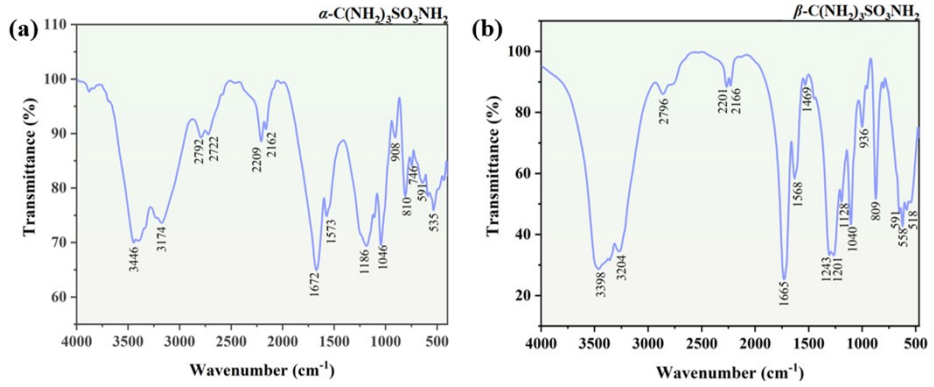

Figure S3. Infrared spectrum of (a) α-$C(NH_2)_3SO_3NH_2$ and (b) β-$C(NH_2)_3SO_3NH_2$.

The results of the infrared spectroscopic tests on α/β-$C(NH_2)_3SO_3NH_2$ are shown in Figure S3. The peak positions of the two compounds are basically the same, which

indicates that both of them possess the same functional groups, consistent with the structural analysis results. The absorption peaks at 3446-2722 cm^{-1} are attributed to the stretching and bending vibrations of N-H. The absorption peaks at 1672-1568 cm^{-1} represents the bending vibration of N-C-N and the stretching vibration of C-NH_2. Overlap of the C-N stretching vibration can be observed at 2209-2162 cm^{-1}. The peaks appearing at 1186-1040 cm^{-1} are attributed to the stretching vibration of the S-O bond. Peaks below 1000 cm^{-1} may include -NH_2 vibrations. The results match those reported in the literature.[28, 31, 32, 45] The Infrared spectrum confirms the presence of [$C(NH_2)_3$] and [SO_3NH_2] groups.

Hirshfeld surface analysis and its corresponding 2D fingerprint plots can be generated in *CrystalExplorer* (version 21.5) by selecting the molecule in question with the mouse and clicking on the Hirshfeld surface icon.[81, 82] Figures S4a and S4c represent the Hirshfeld surface within the normalized contact distance (d_{norm}<3.80 Å). One can clearly find the N-H···O hydrogen bonds in the red regions. Figures S4b and S4d give the shape index surfaces of these two compounds. No triangular-shaped patches above either side of π-conjugated [$C(NH_2)_3$] units are observed in Figures S4b and S4d, implying there are no obvious π-π stacking interactions within these compounds. The reason may be related to the centroid-to-centroid distance of [$C(NH_2)_3$] units being larger than 4.5 Å (Figure 2e and 3f). The 2D fingerprint map quantitatively demonstrates the contribution of different kinds of interactions. As shown in Figures S4e-f, the sum of H···O and N-H contacts account for 61.6% (*α*-$C(NH_2)_3SO_3NH_2$) and 61.2% (*β*-$C(NH_2)_3SO_3NH_2$) of the Hirshfeld surface, respectively. Other intermolecular interactions, such as C-N, C-O, C-C, and N-O, contribute very little (Figures S5 and S6). Therefore, the N-H···O hydrogen bonds in two compounds constitute the primary factor in crystal packing, whereas the π-π stacking may be overlooked.

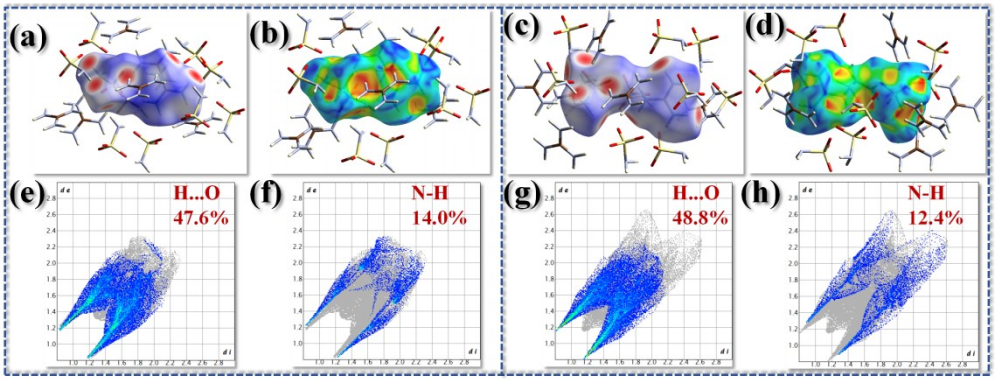

Figure S4. Hirshfeld surface plotted of *α*-$C(NH_2)_3SO_3NH_2$: (a) d_{norm}, (b) shape index, and (e)-(f) 2D fingerprint plots for overall interactions and individual interactions of atom types in crystal packing of *α*-$C(NH_2)_3SO_3NH_2$. Hirshfeld surface plotted of *β*-$C(NH_2)_3SO_3NH_2$: (c) d_{norm}, (d) shape index, and (g)-(h) 2D fingerprint plots.

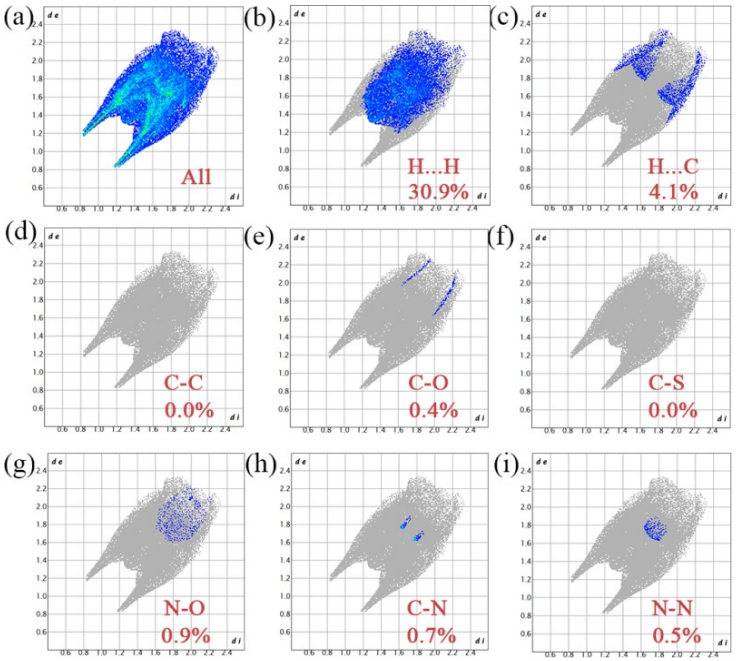

Figure S5. 2D Fingerprint plots for (a) overall interactions and (b–i) individual interactions of atom types of α-$C(NH_2)_3SO_3NH_2$. Here, d_e and d_i represent distances from the Hirshfeld surfaces to the nearest nucleus outside and inside the surface, respectively.

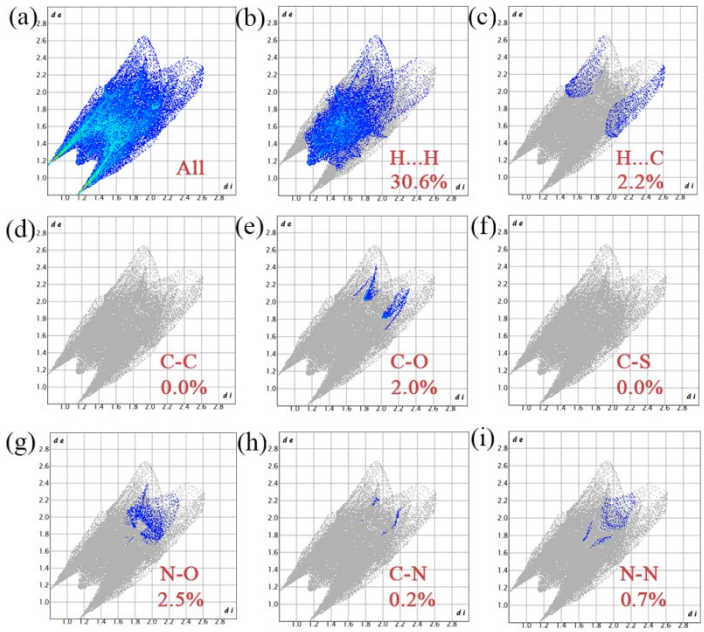

Figure S6. 2D Fingerprint plots for (a) overall interactions and (b–i) individual interactions of atom types of β-$C(NH_2)_3SO_3NH_2$. Here, d_e and d_i represent distances from the Hirshfeld surfaces to the nearest nucleus outside and inside the surface, respectively.

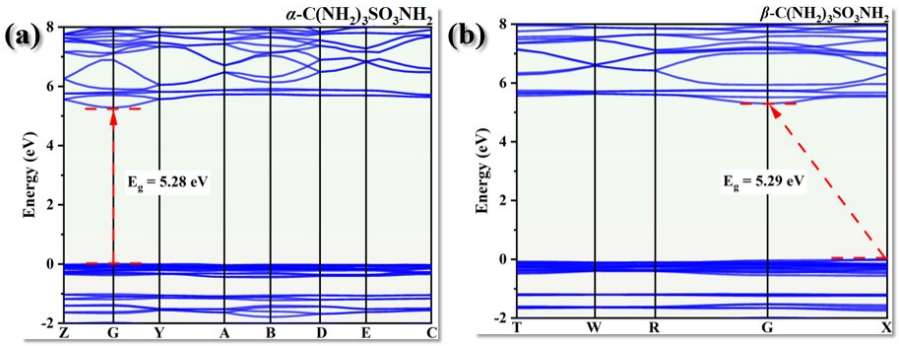

Figure S7. GGA-PBE band structure of (a) α-$C(NH_2)_3SO_3NH_2$ and (b) β-$C(NH_2)_3SO_3NH_2$.

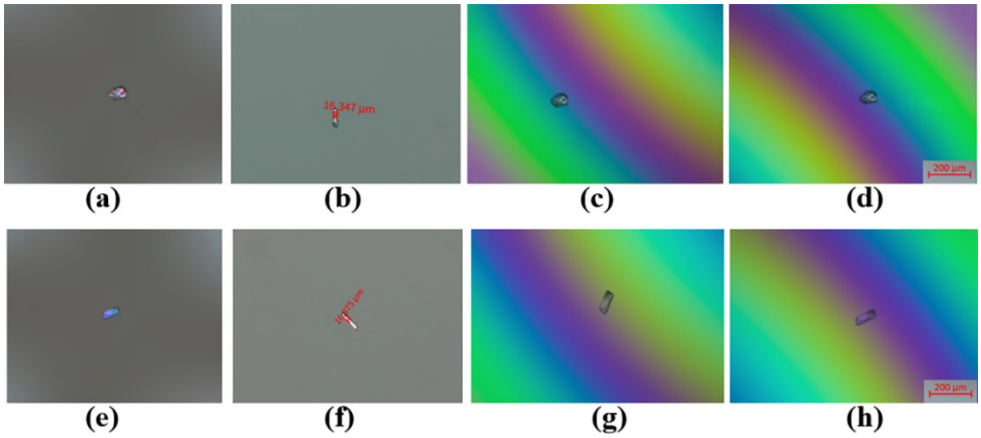

Figure S8. The measurement of birefringence (a) The interference color α-$C(NH_2)_3SO_3NH_2$ and (e) β-$C(NH_2)_3SO_3NH_2$; The thickness of (b) α-$C(NH_2)_3SO_3NH_2$ and (f) β-$C(NH_2)_3SO_3NH_2$ crystal under the polarizing microscope; A α-$C(NH_2)_3SO_3NH_2$ single crystal under the (c) positive (up) and (d) negative (down) compensatory rotation; A β-$C(NH_2)_3SO_3NH_2$ single crystal under the (g) positive (up) and (h) negative (down) compensatory rotation.

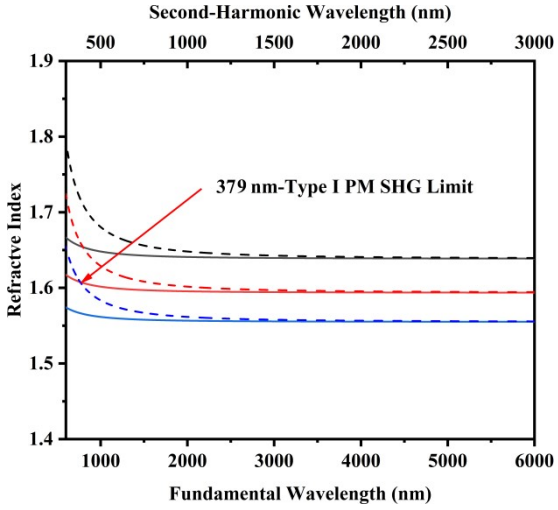

Figure S9. Phase-matched wavelengths of β-$C(NH_2)_3SO_3NH_2$.

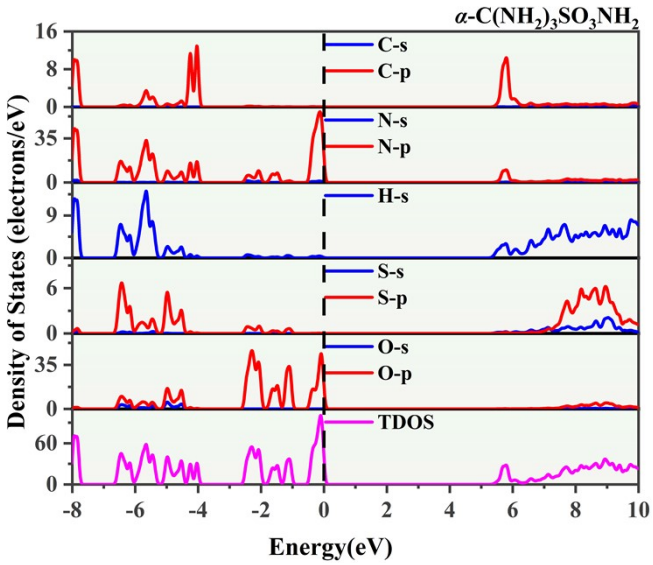

Figure S10. The PDOS of α-$C(NH_2)_3SO_3NH_2$.

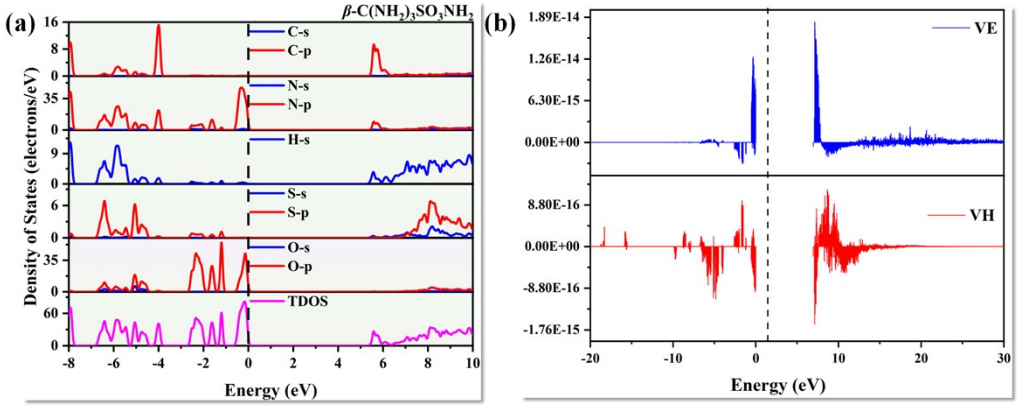

Figure S11. (a)The PDOS of β-$C(NH_2)_3SO_3NH_2$. (b) The occupied states of virtual-electron (VE) and unoccupied states of virtual-hole (VH) of β-$C(NH_2)_3SO_3NH_2$. The contribution of VE is 0.81 pm/V, the contribution of VH is -0.09 pm/V, and the total contribution is 0.72 pm/V. Therefore, the contribution of VE is greater than 70%.

References

1. SAINT, version 7.60A, Bruker Analytical X-ray Instruments, Inc., Madison, WI, 2008.
2. G. Sheldrick, A short history of SHELX, *Acta Crystallogr., Sect. A: Found. Crystallogr.*, 2008, **64**, 112-122.
3. A. Spek, Single-crystal structure validation with the program PLATON, *J. Appl. Crystallogr.*, 2003, **36**, 7-13.
4. L. L. Cao, G. Peng, W. B. Liao, T. Yan, X. F. Long and N. Ye, A microcrystal method for the measurement of birefringence, *CrystEngComm*, 2020, **22**, 1956-1961.
5. D. Vanderbilt, Optimally smooth norm-conserving pseudopotentials, *Phys. Rev. B*, 1985, **32**, 8412-8415.
6. S. J. Clark, M. D. Segall, C. J. Pickard, P. J. Hasnip, M. I. J. Probert, K. Refson and M. C. Payne, First principles methods using CASTEP, *Z Kristallogr. Cryst Mater.*, 2005, **220**, 567-570.
7. W. Kohn, Nobel lecture: electronic structure of matter---wave functions and density functionals, 1999, 77, 1253-1266.
8. J. P. Perdew, K. Burke and M. Ernzerhof, Generalized Gradient Approximation Made Simple, *Phys. Rev. Lett.*, 1996, **77**, 3865-3868.
9. J. S. Lin, A. Qteish, M. C. Payne and V. Heine, Optimized and transferable nonlocal separable ab initio pseudopotentials, *Phys. Rev. B*, 1993, **47**, 4174-4180.
10. A. M. Rappe, K. M. Rabe, E. Kaxiras and J. D. Joannopoulos, Optimized pseudopotentials, *Phys. Rev. B*, 1990, **41**, 1227-1230.
11. D. J. Chadi, Special points for Brillouin-zone integrations, *Phys. Rev. B*, 1977, **16**, 1746-174.
12. J. Heyd and G. E. Scuseria, Assessment and validation of a screened Coulomb hybrid density functional, J. Chem. Phys., 2004, 120, 7274-7280.
13. A. V. Krukau, O. A. Vydrov, A. F. Izmaylov and G. E. Scuseria, Influence of the exchange screening parameter on the performance of screened hybrid functionals, *J. Chem. Phys.*, 2006, **125**.
14. J. Paier, M. Marsman, K. Hummer, G. Kresse, I. C. Gerber and J. G. Ángyán, Screened hybrid density functionals applied to solids, *J. Chem. Phys.*, 2006, **124**.
15. K. T. Chung, Dynamic polarizabilities and refractive indexes of H^- and Li^+ Ions, *Phys. Rev. A*, 1971, **4**, 7-11.
16. W. L. Jia, J. Y. Fu, Z. Y. Cao, L. Wang, X. B. Chi, W. G. Gao and L.-W. Wang, Fast plane wave density functional theory molecular dynamics calculations on multi-GPU machines, *J. Comput. Phys.*, 2013, **251**, 102-115.
17. K. E. Peiponen, V. Lucarini, J. J. Saarinen, E. M. Vartiainen, Kramers-Kronig relations and sum rules of negative refractive index media, Eur. Phys. J. B 41 (2004) 61-65.
18. J. Lin, M.-H. Lee, Z.-P. Liu, C. T. Chen and C. J. Pickard, Mechanism for linear and nonlinear optical effects in β−BaB2O4 crystals, *Phys. Rev. B*, 1999, **60**, 13380-13389.
19. S. N. Rashkeev, W. R. L. Lambrecht and B. Segall, Efficient ab initio method for the calculation of frequency-dependent second-order optical response in semiconductors, *Phys. Rev. B*, 1998, **57**, 3905-3919.
20. B. B. Zhang, M.-H. Lee, Z. H. Yang, Q. Jing, S. L. Pan, M. Zhang, H. P. Wu, X. Su and C.-S. Li, Simulated pressure-induced blue-shift of phase-matching region and nonlinear optical mechanism for $K_3B_6O_{10}X$ (X = Cl, Br), *Appl. Phys. Lett.*, 2015, **106**.
21. S. K. Kurtz and T. T. Perry, A powder technique for the evaluation of nonlinear optical materials, *J. Appl. Phys.*, 1968, **39**, 3798-3813.

22. S. J. Cyvin, J. E. Rauch and J. C. Decius, Theory of Hyper-Raman Effects (Nonlinear Inelastic Light Scattering): Selection Rules and Depolarization Ratios for the Second-Order Polarizability, *J. Chem. Phys.* , 1965, **43**, 4083-4095.
23. X. Cheng, M.-H. Whangbo, G.-C. Guo, M. C. Hong and S. Q. Deng, The Large Second-Harmonic Generation of $LiCs_2PO_4$ is caused by the Metal-Cation-Centered Groups, *Angew. Chem. Int. Ed.*, 2018, **57**, 3933-3937.
24. B. J. B. Schein, E. C. Lingafelter and J. M. Stewart, Redetermination of the structure of the ferroelectric crystal guanidinium aluminum sulfate hexahydrate, GASH, and its Chromium Isomorph, *J. Chem. Phys.*, 1967, **47**, 5183-5189.
25. L. Bohatý, P. Becker, E. Haussühl, I. Němec, O. Lux, H. J. Eichler, H. Yoneda, A. Shirakawa and A. A. Kaminskii, Single crystals of guanidinium zinc sulfate, $[C(NH_2)_3]_2Zn(SO_4)_2$-growth, structure, vibrational spectroscopy and stimulated Raman scattering, *Z. Krist.-Cryst. Mater*, 2015, **230**, 639-649.
26. R. Krupkova, J. Fabry, I. Cisarova and P. Vanek, Redetermination of sulfatotris(thiourea)zinc(II), *Acta Cryst.* , 2007, **63**, m3177-m3178.
27. M. Zdanowska-Frączek, A. Gągor, K. Hołderna-Natkaniec, C. Pawlaczyk, Z. Czapla and P. Ławniczak, Structure, proton conductivity and molecular dynamics of guanidine zinc sulfate, *Solid State Ionics*, 2017, **303**, 113-118.
28. X. H. Dong, Z. Z. Zhang, L. Huang and G. H. Zou, $[C(NH_2)_3]BiCl2SO_4$: an excellent birefringent material obtained by multifunctional group synergy, *Inorg. Chem. Front.*, 2022, **9**, 5572-5578.
29. H. Yang, Z. Y. Wang, C. X. Xu, Y. Lin and G. L. Liu, $La_2B_3O_4(OH)_3(SO_4)_2$: A new rare-earth borate-sulfate with second-harmonic generation response, *J. Solid State Chem.*, 2023, **317**, 123715.
30. D. Y. Dou, Q. Shi, Y. J. Bai, C. Chen, B. B. Zhang and Y. Wang, $C_3N_6H_7SO_3NH_2$: non-π-conjugated tetrahedra decoupling π-conjugated groups achieving large optical anisotropy and wide band gap, *Mater. Chem. Front.*, 2023, **7**, 5924-5931.
31. X. F. Wang, Y. Li, Z. L. Chen, J. Lee, F. F. Zhang, K. R. Poeppelmeier, S. L. Pan and K. M. Ok, $Sr(NO_3)(NH_2SO_3)\cdot H_2O$: first nitrate sulfamate revealing remarkable second harmonic generation and optimized birefringence, *Small Struct.*, 2023, **4**, 2300274.
32. X. Wen, Y. C. Yan, J. Y. Lu, X. M. Shi, P. Tang, J. D. Chen, G. S. Yang, G. Peng, H. H. Yu, H. J. Zhang, Z. G. Hu, J. Y. Wang and N. Ye, $[C_2N_4H_7O][NH_2SO_3]$: High-performance ultraviolet nonlinear optical crystal with ditrigon coupled guanylurea group, *Angew. Chem., Int. Ed.*, 2025, **64**, e202424153.
33. J. R. A. Díaz, G. E. Camí, M. L. González, J. C. Pedregosa and D. R. Vega, Two novel potential anticonvulsant salts of 5-Amino-2-Sulfonamide-1,3,4-Thiadiazole, *J. Chem. Crystallogr.*, 2011, **41**, 1114-1119.
34. M. Arif, X. Liu, Z. J. Li, H. W. Jia, Y. S. Jiang, Z. H. Yang, X. L. Hou and S. L. Pan, Unveiling charge dependent law to enhance birefringence in 2-Aminopyrimidine family, *Adv. Opt. Mater.*, 2025, **13**, 2402327.
35. D. Y. Dou, Q. Shi, H. M. Li, B. B. Zhang, D. Q. Yang and Y. Wang, Rational combination of π-conjugated and non-π-conjugated groups achieving strong nonlinear optical response, large optical anisotropy, and UV light-switchable fluorescence, Adv. Sci., 2024, **11**, 2401325.
36. M. Arif, X. Liu, H. W. Jia, Z. H. Yang, X. L. Hou and S. L. Pan, Optimizing optical anisotropy in low-dimensional structures via intralayer hydrogen bonding modulation and anionic substitution, *Mater. Horiz.*, 2025, **12**, 3538-3545.

37. H. Zhou, M. Cheng, D. D. Chu, X. Liu, R. An, S. L. Pan and Z. H. Yang, Sulfate derivatives with heteroleptic tetrahedra: new deep-ultraviolet birefringent materials in which weak interactions modulate functional module ordering, *Angew. Chem. Int. Ed.* , 2025, **64**, e202413680.
38. Y. Li, X. L. Chen and K. M. Ok, Strategically designed metal-free deep-ultraviolet birefringent crystals with superior optical properties, *Chem. Sci.*, 2024, **15**, 15145-15151.
39. Z.-P. Zhang, X. Liu, R.-X. Wang, S. Zhao, W.-J. He, H.-Y. Chen, X.-B. Deng, L.-M. Wu, Z. Y. Zhou and L. Chen, Remarkable second harmonic generation response in $(C_5H_6NO)^+(CH_3SO_3)^-$: unraveling the role of hydrogen bond in thermal driven nonlinear optical switch, *Angew. Chem. Int. Ed.*, 2024, **63**, e202408551.
40. M. Luo, C. S. Lin, D. H. Lin and N. Ye, Rational design of the metal-free $KBe_2BO_3F_2$·(KBBF) family Member $C(NH_2)_3SO_3F$ with ultraviolet optical nonlinearity, *Angew. Chem., Int. Ed.*, 2020, **59**, 15978-15981.
41. Y. C. Liu, X. M. Liu, Z. Y. Xiong, B. W. Liu, J. L. Xu, L. Li, S. G. Zhao, Z. S. Lin, M. C. Hong and J. H. Luo, 2D van der waals layered $[C(NH_2)_3]_2SO_3S$ exhibits desirable uv nonlinear-optical trade-off, *Inorg. Chem.*, 2021, **60**, 14544-14549.
42. Y. C. Liu, Y. Q. Liu, Z. S. Lin, Y. Q. Li, Q. R. Ding, X. Chen, L. Li, S. G. Zhao, M. C. Hong and J. H. Luo, Nonpolar $Na_{10}Cd(NO_3)_4(SO_3S)_4$ exhibits a large second-harmonic generation, *CCS Chem.*, 2022, **4**, 526-531.
43. H. Y. Sha, D. L. Yang, Y. R. Shang, Z. J. Wang, R. B. Su, C. He, X. M. Yang and X. F. Long, Trithionic guanidine: A novel semi-organic short-wave ultraviolet nonlinear optical sulfate with dimeric heteroleptic tetrahedra, *Chin. Chem. Lett.*, 2025, **36**, 109730.
44. M. Zhang, B. B. Zhang, D. Q. Yang and Y. Wang, $[C(NH_2)_3]_2S_2O_8$: combining delocalized and localized π-conjugate units to achieve strong optical anisotropy, *Inorg. Chem. Front.*, 2022, **9**, 6067-6074.
45. S. Y. Li, D. Y. Dou, C. Chen, Q. Shi, B. B. Zhang and Y. Wang, $[C(NH_2)_3]_2S_2O_6$: A SBBO-like dithionate crystal with large optical anisotropy, *Inorg. Chem.*, 2024, **63**, 24076-24082.
46. X. F. Wang, X. D. Leng, Y. Kuk, J. Lee, Q. Jing and K. M. Ok, Deep-ultraviolet transparent mixed metal sulfamates with enhanced nonlinear optical properties and birefringence, *Angew. Chem. Int. Ed.*, 2024, **63**, e202315434.
47. C. C. Jin, H. Zeng, F. Zhang, H. T. Qiu, Z. H. Yang, M. Mutailipu and S. L. Pan, Guanidinium fluorooxoborates as efficient metal-free short-wavelength nonlinear optical crystals, *Chem. Mater.*, 2022, **34**, 440-450.
48. X. Hao, M. Luo, C. S. Lin, G. Peng, F. Xu and N. Ye, $M(NH_2SO_3)_2$ (M=Sr, Ba): two deep-ultraviolet transparent sulfamates exhibiting strong second harmonic generation responses and moderate birefringence, *Angew. Chem., Int. Ed.*, 2021, **60**, 7621-7625.
49. Y. J. Fan, L. Zhong, H. T. Tian, C. S. Lin, L. L. Wu, T. Yan and M. Luo, Designing a novel perovskite-type $KCd(NH_2SO_3)_3$ with deep-ultraviolet transparency and strong second-harmonic generation response, *Inorg. Chem. Front.*, 2025, **12**, 1656-1661.
50. M. Mutailipu, J. Han, Z. Li, F. M. Li, J. J. Li, F. F. Zhang, X. F. Long, Z. H. Yang and S. L. Pan, Achieving the full-wavelength phase-matching for efficient nonlinear optical frequency conversion in $C(NH_2)_3BF_4$, *Nat. Photon.*, 2023, **17**, 694-701.
51. C. H. Hu, M. F. Wu, M. Zhang, J. Han, X. L. Hou, F. Zhang, Z. H. Yang and S. L. Pan, "Cation Activation": An effective strategy for the enhancement of birefringence, *Adv. Optical Mater.*, 2023, **11**, 2300579.

52. Z. Q. Chen, F. M. Li, Z. H. Yang, S. L. Pan and M. Mutailipu, Hydroxyfluorooxoborate $(NH_4)[C(NH_2)_3][B_3O_3F_4(OH)]$ for exploring the effects of cation substitution on structure and optical properties, *Chem. Commun.*, 2023, **59**, 12435-12438.
53. Y. X. Song, M. Luo, D. H. Lin, C. S. Lin, Z. J. Wang, X. F. Long and N. Ye, π-Conjugated trigonal planar $[C(NH_2)_3]^+$ cationic group: A superior functional unit for ultraviolet nonlinear optical materials, *ACS Omega*, 2021, **6**, 9263-9268.
54. C. Wu, X. X. Jiang, Z. J. Wang, H. Y. Sha, Z. S. Lin, Z. P. Huang, X. F. Long, M. G. Humphrey and C. Zhang, UV solar-blind-region phase-matchable optical nonlinearity and anisotropy in a π-conjugated cation-containing phosphate, *Angew. Chem., Int. Ed.*, 2021, **60**, 14806-14810.
55. D. Y. Dou, B. J. Cai, B. B. Zhang and Y. Wang, $M(NH_2SO_3)_2{\cdot}xH2O$ (M = Ca, Pb, x = 0, 1, 4): effect of hydrogen bonding on structural transformations and second harmonic generation of metal sulfamates, *Inorg. Chem.*, 2022, **61**, 21131-21138.
56. Z. Y. Bai, L. H. Liu, Z. B. Lin and K. M. Ok, $[C(NH_2)_3]_2Zn(CO_3)_2$: a guanidinium-templated ultraviolet nonlinear optical material, *Inorg. Chem.*, 2022, **61**, 12473-12480.
57. X. F. Wang, J. Lee, Y. Li, Y. Kuk and K. M. Ok, $Cd(NH_2SO_3)_2{\cdot}xH_2O$ (x = 0, 2): new sulfamates with a unique coordination environment and reversible phase transitions, *Inorg. Chem. Front.*, 2023, **10**, 1411-1420.
58. Z. Y. Bai, Y. Kuk, J. Lee, H. Kim and K. M. Ok, Guanidinium vanadate $[C(NH_2)_3]_3VO_4{\cdot}2H_2O$ Revealing enhanced second-harmonic generation and wide band gaps, *Inorg. Chem.*, 2024, **63**, 3578-3585.
59. J.-X. Wang, S.-F. Li, M.-M. Ren, M.-H. Lv, R.-L. Tang, J. Chen, H. B. Huang, B. B. Zhang and D. Yan, $[C(NH_2)_3][B(C_2O_2H_4)_2]$: an organic–inorganic hybrid borate containing nonlinear-optical active unit $[B(C_2O_2H_4)_2]^-$ with Solar-blind-region optical nonlinearity, *Inorg. Chem.*, 2024, **63**, 4487-4491.
60. J. H. Cui, S. B. Wang, A. Tudi, M. Q. Gai, Z. H. Yang and S. L. Pan, $(C(NH_2)_3)_2(I_2O_5F)(IO_3)(H_2O)$ and $C(NH_2)_3IO_2F_2$: two guanidine fluorooxoiodates with wide band gap and large birefringence, *Inorg. Chem.* , 2024, **63**, 661-667.
61. M. Zhang, B. B. Zhang, D. Q. Yang and Y. Wang, Synergistic effect of π-conjugated $[C(NH_2)_3]$ cation and sb(iii) lone pair stereoactivity on structural transformation and second harmonic generation, *Inorg. Chem.*, 2021, **60**, 18483-18489.
62. N. I. Sorokina, V. V. Ilyukhin and N. V. Belov, The crystal structure of guanido iodate $C(NH_2)_3IO_3$, *Sov. Phys. Dokl.*, 1977, **22**, 555.
63. X. H. Dong, Y. Long, L. Huang, L. L. Cao, D. J. Gao, J. Bi and G. H. Zou, Large optical anisotropy differentiation induced by the anion-directed regulation of structures, *Inorg. Chem. Front.*, 2022, **9**, 6441-6447.
64. X. Wen, C. S. Lin, M. Luo, H. X. Fan, K. C. Chen and N. Ye, $[C(NH_2)_3]_3PO_4{\cdot}2H_2O$: A new metal-free ultraviolet nonlinear optical phosphate with large birefringence and second-harmonic generation response, *Sci. China Mater.* , 2021, **64**, 2008-2016.
65. D. Yan, M.-M. Ren, Q. Liu, F.-F. Mao, Y. Ma, R.-L. Tang, H. B. Huang, B. B. Zhang, X.-D. Zhang and S.-F. Li, $[C(NH_2)_2NHNO_2][C(NH_2)_3](NO_3)_2$: a mixed organic cationic hybrid nitrate with an unprecedented nonlinear-optical-active unit, *Inorg. Chem.*, 2023, **62**, 4757-4761.
66. D. Zhang, Q. Wang, L. Y. Ren, L. L. Cao, L. Huang, D. J. Gao, J. Bi and G. H. Zou, Sharp Enhancement of birefringence in antimony oxalates achieved by the cation–anion synergetic interaction strategy, *Inorg. Chem.* , 2022, **61**, 12481-12488.
67. D. Yan, M.-M. Ren, F.-F. Mao, Y. Ma, R.-L. Tang, B. B. Zhang, Y. Ma, X.-D. Zhang and S.-F. Li, $C(NH_2)_3(I_3O_8)(HI_3O_8)(H_2I_2O_6)(HIO_3)_4{\cdot}3H_2O$: An unprecedented asymmetric guanidinium polyiodate

with a strong second-harmonic-generation response and a wide band gap, *Inorg. Chem.*, 2023, **62**, 1323-1327.

68. X. J. Qiao, X. M. Liu, L. Bayarjargal, A. J. Corkett, W. Y. Wang, Z. L. Ma, Z. S. Lin and R. Dronskowski, Nonlinear optical effects in two mercury cyanamide/guanidinium chlorides $Hg_3(NCN)_2Cl_2$ and $Hg_2(C(NH_2)_3)Cl_5$, *J. Mater. Chem. C*, 2021, **9**, 967-974.
69. M.-H. Lv, S.-F. Li, M.-M. Ren, J.-X. Wang, R.-L. Tang, J. Chen, H. B. Huang, B. B. Zhang and D. Yan, $[C(NH_2)_3]_6Mo_7O_{24}$: A guanidinium molybdate as a uv nonlinear optical crystal with large birefringence, *Inorg. Chem.*, 2024, **63**, 3948-3954.
70. Y. Zhang, M.-H. Lv, S.-F. Li, H. B. Huang, B. B. Zhang and D. Yan, $[C(NH_2)_3]_{10}(MoO_3)_{10}(PO_4)_2(HPO_4)_2{\cdot}5H_2O$: Synergy effect of multiple functional units results in significant birefringence, *J. Solid State Chem.*, 2024, **337**, 124823.
71. W. Zeng, Y. Tian, X. H. Dong, L. Huang, H. M. Zeng, Z. E. Lin and G. H. Zou, $C(NH_2)_3MoO_3(IO_3)$: A molybdenyl iodate with giant birefringence designed via a cation–anion synergetic interaction strategy, *Chem. Mater.*, 2024, **36**, 2138-2146.
72. W. Xu, L. Ma, Y.-L. Lv, S.-Y. Ma, W. L. Liu, S.-P. Guo and R.-L. Tang, $C(NH_2)_3Cd(C_2O_4)Cl(H_2O){\cdot}H_2O$ and $BaCd(C_2O_4)_{1.5}Cl(H_2O)_2$: two oxalate chlorides obtained by chemical scissors strategy exhibiting low-dimensional structural networks and balanced overall optical properties, *Inorg. Chem.*, 2024, **63**, 67-72.
73. M. J. Li, Z. Y. Wang, B. Ahmed, Y. Q. Li, H. Wang, Y. P. Song, X. Y. Song, X. J. Kuang, J. H. Luo and S. G. Zhao, A second-order nonlinear optical material consisting of two π-conjugated groups, *ChemPlusChem*, 2023, **88**, e202300094.
74. D. Yan, Y. Ma, R.-L. Tang, L. Hu, F.-F. Mao, J. Zheng, X.-D. Zhang and S.-F. Li, $C(NH_2)_3Rb(I_3O_8)(IO_3)(I_2O_6H_2)$: An unprecedented organic–inorganic hybrid polyiodate with two different polyiodate groups, *J. Solid State Chem.*, 2022, **315**, 123530.
75. H. M. Wang, Q. Wang, Q. Wang, L. L. Cao, L. Huang, D. J. Gao, J. Bi and G. H. Zou, Yin–Yang Complementarity strategy achieving giant optical anisotropy in a metal-free birefringent material $C(NH_2)_3(HC_4O_4)$, *Cryst. Growth Des.*, 2022, **22**, 4236-4242.
76. W. Y. Zhang, Z. C. Li, X. D. Leng, Q. Jing and Q. Wen, Enhancement of birefringence in π-conjugated oxyfluorides achieved via van der waals layered structural optimization, *Cryst. Growth Des.*, 2024, **24**, 3140-3148.
77. C. T. Chen, Z. Y. Xu, D. Q. Deng, J. Zhang, G. K. L. Wong, B. C. Wu, N. Ye and D. Y. Tang, The vacuum ultraviolet phase-matching characteristics of nonlinear optical $KBe_2BO_3F_2$ crystal, *Appl. Phys. Lett.*, 1996, **68**, 2930-2932.
78. C. T. Chen, Y. C. Wu, A. D. Jiang, B. C. Wu, G. M. You, R. K. Li and S. J. Lin, New nonlinear-optical crystal: LiB_3O_5, *J. Opt. Soc. Am. B*, 1989, **6**, 616-621.
79. J.-M. Tu and D. A. Keszler, $CsLiB_6O_{10}$: A noncentrosymmetric polyborate, *Mater. Res. Bull.*, 1995, **30**, 209-215.
80. C. Chen, W. Bochard and J. Aidong, A new-type ultraviolet SHG crystal β-BaB_2O_4, *Sci. Sin. B*, 1985.
81. M. A. Spackman and D. Jayatilaka, Hirshfeld surface analysis, *CrystEngComm,*, 2009, **11**, 19-32.
82. P. R. Spackman, M. J. Turner, J. J. McKinnon, S. K. Wolff, D. J. Grimwood, D. Jayatilaka and M. A. Spackman, CrystalExplorer: a program for Hirshfeld surface analysis, visualization and quantitative analysis of molecular crystals, *J. Appl. Cryst.* , 2021, **54**, 1006-1011.